Biomechanics-informed Non-rigid Medical Image Registration and its Inverse Material Property Estimation with Linear and Nonlinear Elasticity

Zhe Min[1,2(✉)], Zachary M. C. Baum[2], Shaheer U. Saeed[2], Mark Emberton[3], Dean C. Barratt[2], Zeike A. Taylor[4], and Yipeng Hu[2]

[1] School of Control Science and Engineering, Shandong University, Jinan, China
minzhe@sdu.edu.cn;z.min@ucl.ac.uk
[2] Centre for Medical Image Computing and Wellcome/EPSRC Centre for Interventional & Surgical Sciences, University College London, London, UK
[3] Division of Surgery & Interventional Science, University College London, London, UK
[4] CISTIB Centre for Computational Imaging and Simulation Technologies in Biomedicine, Institute of Medical and Biological Engineering, University of Leeds, Leeds, UK

Abstract. This paper investigates both biomechanical-constrained non-rigid medical image registrations and accurate identifications of material properties for soft tissues, using physics-informed neural networks (PINNs). The nonlinear elasticity theory is leveraged to formally establish the partial differential equations (PDEs) representing physics laws of biomechanical constraints to be satisfied, with which registration and identification tasks are treated as forward (i.e., data-driven solutions of PDEs) and inverse (i.e., parameter estimation) problems under PINNs respectively. While the forward problem has direct clinical applications in guiding targeted biopsy and treatment, the solution to the inverse problem may open new research directions in quantifying disease-indicative mechanical properties of *in vivo* tissues. Two net configurations (i.e., Cfg1 and Cfg2) have also been compared for both linear and nonlinear physics models, according to whether backbones are shared between branches or not. Two sets of experiments have been conducted, using pairs of undeformed and deformed MR images from clinical cases of prostate cancer biopsy. In the first experiment, against the finite-element-computed ground-truth, the root mean squared error (rmse) of registration for surface points was reduced from 1.83±0.51 mm without PINNs to 1.43±0.70 mm (Cfg1, $p = 0.024$) and 1.23 ± 0.69 mm (Cfg2, $p < 0.001$) with linear elasticity, and to 1.45 ± 0.84 mm (Cfg1, $p = 0.004$) and 1.24 ± 0.69 mm (Cfg2, $p < 0.001$) with nonlinear elasticity, while average differences between linear and nonlinear models were not found statistically significant (e.g., $p = 0.972$ between two Cfg1s) but their respective benefits may depend on specific patients. In the second experiment, the nonlinear model exhibited evident advantages over the linear counterpart ($p = 0.002$) in predicting ratios of tissue stiffness (i.e., Young's modulus) between two subregions (i.e., peripheral and transition zones) of the prostate, with the mean average percentage error (mAPE) values

being 14.20%±14.12% and 76.28%±30.97%, respectively. The codes are available at https://github.com/ZheMin-1992/Registration_PINNs.

Keywords: Medical image registration · Biomechanical constraints · Physics-informed neural networks · Material property estimation.

1 Introduction

Biomechanical modelling plays an important role in regularising medical image registration [1,26,27] that further enables surgical guidance for different organs (e.g., prostate [1,7,24,28], liver [17], brain [10,11] and heart [19]), for example, to constrain predicted spatial transformations to be physically plausible, under either iterative optimisation [24] or neural-network-training [7,28] schemes. Biomechanical constraints could vary from simple linear [12] to complex nonlinear models [1,15], while they require values of material properties if applied to the registration problem. This paper investigates both aspects by leveraging the capabilities of physics-informed neural networks (PINNs) to seek data-driven solutions (i.e., forward problem) and enable data-driven discovery (i.e., inverse problem) of partial differential equations (PDEs) [9] respectively, in the non-rigid medical image registration and material property estimation.

Linear elasticity models assuming a linear relationship between stress and strain, are only effective for modelling small deformations under low-stress conditions [12]. Nonlinear elasticity models built on more complex constitutive models and strain energy functions, are better suited for capturing large deformations and nonlinear material behavior [12]. For example, the anisotropic viscoelasticity constitutive models [4,13,15] were utilised for simulating soft tissues' deformations, led to more realistic organ (e.g., liver) geometries than linear models with desired properties such as stress dissipation [23]. The nonlinear finite-element-analysis was developed for modelling-fidelity surgical simulations [22]. However, the choices of hyperviscoelastic, hyperelastic, and linear elastic constitutive models were demonstrated to be not important in estimating brain shifts for an image-guided neurosurgery procedure [25]. *It is unclear whether a more complex nonlinear model (i.e., both geometrical and constitutive models) could make a difference in the non-rigid point set registration problem.*

Material property estimation aims to quantify mechanical properties of materials (e.g., soft tissues), which can be used to develop customized surgical plans that could improve surgical outcomes [5,6]. Perhaps more interestingly, it may assist disease detection and localisation, as studies frequently found *in vitro* tumour has distinct mechanical properties compared to the healthy tissue [8]. The identifications of bulk and shear modulus, under both linear elasticity and hyperelasticity models, were explored using specimens with simple one-or-two layers structures through experimental tests (e.g., uniaxial tension or compression) [3]. The authors revealed multiple findings about under what conditions parameters are identifiable, for example, to compute material parameters of a single-layered specimen, a uniaxial tensile test either together with lateral strain

measurement, with torsion or with a shear experiment is needed [3]. We note that circumstances are much more complicated in both soft-tissue deformation modelling where exact values of stress and strain are unknown, and image registration where displacement vectors of voxels need to be estimated. *It is thus unknown whether material properties are identifiable or not, within the challenging scenario of image registration where boundary conditions also need to be estimated.*

To answer the first question of whether nonlinear elasticity models are better than linear counterparts in registration, in a similar fashion with a recent work [14] where linear elasticity was adopted, this study incorporates nonlinear biomechanical constraints in forms of PDEs into a PINN for registration. The findings first confirmed the validity of adopting PINNs to impose biomechanical constraints for predicted transformations and to reduce registration error, and also indicated that there existed no statistically significant difference between average performances using linear and nonlinear models while choices may depend on specific patients. To answer the second question of whether material properties are identifiable along with registration, PINNs were utilised to formulate the joint optimisation framework of the registration problem and the material property estimation problem. The results demonstrated that ratios of soft tissues' stiffness (i.e., Young's modulus) between two distinct compartments (i.e.,the peripheral zone and transition zone) of the prostate gland could be successfully recovered, while nonlinear models exhibited evident advantages over their linear counterparts in this problem.

Our contributions are summarised as follows. **1)** We developed a learning-based biomechanical-constrained non-rigid registration algorithm using PINNs, where linear elasticity is generalised to the nonlinear version. **2)** We demonstrated extensively that nonlinear elasticity shows no statistical significance against linear models in computing point-wise displacement vectors but their respective benefits may depend on specific patients, with finite-element (FE) computed ground-truth. **3)** We formulated and solved the inverse parameter estimation problem, under the joint optimisation scheme of registration and parameter identification using PINNs, whose solutions can be accurately found by locating saddle points of the optimisation.

2 Methods

The non-rigid 3D point set registration problem in fields of medical imaging, is to warp the source point set $\mathbf{P}_{\mathcal{S}} \in \mathbb{R}^{N_s \times 3}$ with $\mathbf{p}_s \in \mathbb{R}^3$ to the target point set $\mathbf{P}_{\mathcal{T}} \in \mathbb{R}^{N_t \times 3}$ with $\mathbf{p}_t \in \mathbb{R}^3$, so as to accurately map important anatomical structures in two spaces. The warped source point set is $\mathsf{T}(\mathbf{P}_{\mathcal{S}}) = \mathbf{P}_{\mathcal{S}} + \mathbf{D}_{\mathcal{S}}$, where the displacement vectors are $\mathbf{D}_{\mathcal{S}} \in \mathbb{R}^{N_s \times 3}$ with $\mathbf{d}_s \in \mathbb{R}^3$.

The idea of imposing biomechanical constraints in the registration problem with physics-informed neural networks (PINNs), like that in [14], is to predict point-wise displacement vectors and biomechanical-related values (e.g., stress or strain), of which the underlying physics laws (i.e., governing equations) usu-

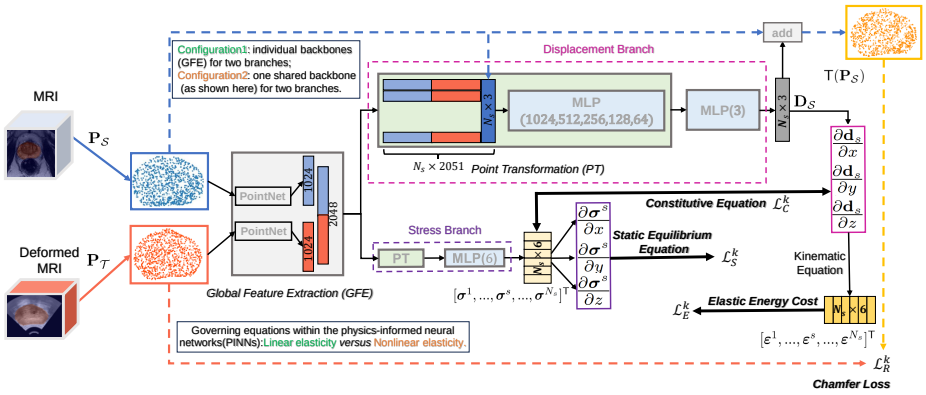

Fig. 1. The schematic of the proposed physics-informed neural networks.

ally represented by partial differential equations (PDEs) should be satisfied. As shown in Fig. 1 and introduced in details in Sect. 2.3, there are three main governing equations and one energy function in modelling deformation of soft tissues, from simple linear relationships [14], to the elaborate nonlinear cases (i.e., compressible Neo-Hookean model [16]) in this study. Let $\mathcal{D}_k$ be the data set of k-th patient, containing $\mathbf{P}_\mathcal{S}$ and $\mathbf{P}_\mathcal{T}$, Fig. 1 shows the algorithm schematic where the displacement-predicting branch is $g_{\theta_g}(\mathcal{D}_k)$ and the stress-predicting branch is $h_{\theta_h}(\mathcal{D}_k)$ with learnable parameters θ_g and θ_h, which together constitutes $e_\theta(\mathcal{D}_k)$ with θ. Two net configurations have been compared, where individual and shared (as depicted in Fig. 1) backbones (i.e., global feature extraction module based on PointNet [18]) are utilised to extract features for two branches respectively. For clarity, the four models with two net configurations and two physics models are denoted as Linear Cfg1, Linear Cfg2, Nonlinear Cfg1 and Nonlinear Cfg2.

2.1 The Forward Problem of Non-Rigid Point Set Registration using PINNs

The registration task is formulated as the forward problem (i.e., the data-driven solutions of PDEs) which estimates the unknown function $g_{\theta_g}(\mathcal{D}_k)$ within the PINNs framework where nonlinear PDEs are parameterised by lame parameters $\lambda_s \in \mathbb{R}$ and $\mu_s \in \mathbb{R}$ at the point $\mathbf{p}_s$. Here, boundary conditions are 'actual' displacement vectors of source points which are unknown and thus their estimation errors are approximated with the Chamfer loss. The Chamfer loss $\mathcal{L}_R^k(\theta_g; \mathcal{D}_k)$ first seeks the nearest point in the other point set (e.g., $\mathsf{T}(\mathbf{P}_\mathcal{S})$) to each point in one point set(e.g., $\mathbf{P}_\mathcal{T}$) and computes the L2 distance, repeats the above operation for the other point set $\mathsf{T}(\mathbf{P}_\mathcal{S})$ and returns the sum of average distances. The Chamfer loss can be either applied to all points $\mathbf{P}_\mathcal{S}$ and $\mathbf{P}_\mathcal{T}$ or surface points only $\mathbf{P}_\mathcal{S}^{\text{surface}} \in \mathbb{R}^{N_s^{\text{surface}} \times 3}$ and $\mathbf{P}_\mathcal{T}^{\text{surface}} \in \mathbb{R}^{N_t^{\text{surface}} \times 3}$ (i.e., 'strict' boundary conditions where surface points are points on the boundary). By regarding all points as 'collocation' points following PINNs notation conventions [20], as shown in

Fig. 1, nonlinear PDEs include the static equilibrium deviation loss $\mathcal{L}_S^k(\theta_h; \mathcal{D}_k) = \sum_{s=1}^{N_s} f_{\text{static}}(\frac{\partial \boldsymbol{\sigma}^s}{\partial x}, \frac{\partial \boldsymbol{\sigma}^s}{\partial y}, \frac{\partial \boldsymbol{\sigma}^s}{\partial z})$ that regularizes spatial derivatives of stress $\boldsymbol{\sigma}^s$, the constitutive deviation loss $\mathcal{L}_C^k(\theta; \mathcal{D}_k) = \sum_{s=1}^{N_s} f_{\text{const}}(\boldsymbol{\sigma}^s, \frac{\partial \mathbf{d}_s}{\partial \mathbf{p}_s}, \lambda_s, \mu_s)$ that relates $\boldsymbol{\sigma}^s$ and spatial derivatives of displacements $\frac{\partial \mathbf{d}_s}{\partial \mathbf{p}_s}$ with λ_s and μ_s, and the elastic energy loss $\mathcal{L}_E^k(\theta_h; \mathcal{D}_k) = \sum_{s=1}^{N_s} f_{\text{energy}}(\boldsymbol{\varepsilon}^s, \lambda_s, \mu_s)$ that relies on strains and lame parameters. Note that $f_{\text{static}}(\star)$, $f_{\text{const}}(\star)$ and $f_{\text{energy}}(\star)$ will be defined in Sect. 2.3. The training loss $\mathcal{L}^k(\theta; \mathcal{D}_k)$ in the forward problem for the k-th subject is given by a $(w \in \mathbb{R}^+)$-weighted sum of these terms,

$$\mathcal{L}^k(\theta; \mathcal{D}_k) = w\mathcal{L}_R^k(\theta_g; \mathcal{D}_k) + \mathcal{L}_S^k(\theta_h, \mathcal{D}_k) + \mathcal{L}_C^k(\theta; \mathcal{D}_k) + \mathcal{L}_E^k(\theta_h; \mathcal{D}_k), \quad (1)$$

where $\mathcal{D}_k$ is considered to include lamé parameters λ_s and μ_s.

2.2 The Inverse Problem of Identifying Material Properties of Soft Tissues using PINNs

In Sect. 2.1, we treat the registration as the forward problem using PINNs, which necessitates knowing material properties (e.g., Young's modulus). In contrast, the parameter (e.g., material properties) estimation is regarded as the inverse problem (i.e., the data-driven discovery of PDEs) under a similar PINNs framework. Consider two distinct compartments of the prostate gland, i.e., the peripheral zone (PZ) and transition zone (TZ), which exhibit different stiffness magnitudes [6,5]. Let $\mathcal{D}_k^{\text{PZ}}$ and $\mathcal{D}_k^{\text{TZ}}$ denote points in PZ and TZ, $E_k^{\text{PZ}} \in \mathbb{R}$ and $E_k^{\text{TZ}} \in \mathbb{R}$ be their respective Young's modulus values. The particular example of the inverse problem here, assuming that E_k^{TZ} is known, is to estimate the ratio $\beta_k \in \mathbb{R}$ of E_k^{PZ} to E_k^{TZ}, which plays an important role in biomechanics-constrained non-rigid point set registration as verified in [6]. To this end, one learnable weight that functions as β_k is added into the network $e_\theta(\mathcal{D}_k)$. The loss function for the inverse problem, under the joint learning scheme of point set registration and parameter estimation, is

$$\mathcal{L}^k(\theta, \beta_k; \mathcal{D}_k) = w\mathcal{L}_R^k(\theta_g; \mathcal{D}_k) + \mathcal{L}_S^k(\theta_h, \mathcal{D}_k) + \mathcal{L}_C^k(\theta, \beta_k; \mathcal{D}_k) + \mathcal{L}_E^k(\theta_h, \beta_k; \mathcal{D}_k), \quad (2)$$

where $\mathcal{L}_C^k(\theta, \beta_k; \mathcal{D}_k)$ and $\mathcal{L}_E^k(\theta, \beta_k; \mathcal{D}_k)$ can be expanded as $\mathcal{L}_{C/E}^k(\theta, \beta_k; \mathcal{D}_k) \equiv \mathcal{L}_{C/E}^k(\theta; \mathcal{D}_k^{\text{TZ}}, E_k^{\text{TZ}}) + \mathcal{L}_{C/E}^k(\theta; \mathcal{D}_k^{\text{PZ}}, \beta_k E_k^{\text{TZ}})$, where lame parameters λ_s and μ_s at $\mathbf{p}_s$ are computed using E_k^{TZ} and $\beta_k E_k^{\text{TZ}}$ depending on the sub-regions (i.e., $\mathcal{D}_k^{\text{PZ}}$ or $\mathcal{D}_k^{\text{TZ}}$) in which $\mathbf{p}_s$ falls.

The optimisation problem minimising $\mathcal{L}^k(\theta, \beta_k; \mathcal{D}_k)$ in Eq. (2) is likely to be ill-posed, in that it contains unknowns in both registration-related and physics-laws-related loss terms (i.e., PDEs). Instead of seeking local minimums w.r.t. material parameters which is likely to be unidentifiable and produces naive solutions, we investigate saddle points that are much more interesting and represent practically meaningful solutions as will be demonstrated in Sect. 3.

2.3 Governing Equations for Deforming Soft Tissues Considering Nonlinear Elasticity

In this section, we describe in details PDEs representing governing equations in both the forward problem in Sect. 2.1 and the inverse problem in Sect. 2.2.

Nonlinear Strain-displacement Equations The nonlinear strain-displacement equation at a source point $\mathbf{p}_s$ is

$$\boldsymbol{\varepsilon}^s = \frac{1}{2}(\nabla \mathbf{d}_s + \nabla \mathbf{d}_s^\mathsf{T} + \nabla \mathbf{d}_s^\mathsf{T} \nabla \mathbf{d}_s), \tag{3}$$

where $\boldsymbol{\varepsilon}^s$ is the *Green-Lagrangian strain* tensor at $\mathbf{p}_s$, $\nabla \mathbf{d}_s$ is the displacement gradient w.r.t. spatial coordinates x, y, z of $\mathbf{p}_s$. As shown in Fig. 1, Eq. (3) is utilised to derive point-wise strain $\boldsymbol{\varepsilon}^s$ from the predicted displacement vector $\mathbf{d}_s$.

Static Equilibrium Equations In nonlinear elasticity, $\boldsymbol{\sigma}^s$ predicted by $h_{\theta_h}(\mathcal{D}_k)$ at $\mathbf{p}_s$ would be a *2nd Piola-Kirchhoff stress* tensor, satisfy the following equilibrium equation $\sigma^s_{ji,j} + F_i = 0$ where $(\cdot)_{,j}$ is a shorthand for $\frac{\partial(\cdot)}{\partial(\mathbf{p}_s)_j}$, $F_i \in \mathbb{R}$ is the body force that is assumed to be zero at the static equilibrium, i and j denote three spatial directions. The PDEs that compose $\mathcal{L}^k_S(\theta_h; \mathcal{D}_k)$ in Eqs. (1) and (2) are $f_{\text{static}}(\frac{\partial \boldsymbol{\sigma}^s}{\partial x}, \frac{\partial \boldsymbol{\sigma}^s}{\partial y}, \frac{\partial \boldsymbol{\sigma}^s}{\partial z}) = ||\frac{\partial \sigma^s_{xx}}{\partial x} + \frac{\partial \sigma^s_{yx}}{\partial y} + \frac{\partial \sigma^s_{zx}}{\partial z}||_2^2 + ||\frac{\partial \sigma^s_{xy}}{\partial x} + \frac{\partial \sigma^s_{yy}}{\partial y} + \frac{\partial \sigma^s_{zy}}{\partial z}||_2^2 + ||\frac{\partial \sigma^s_{xz}}{\partial x} + \frac{\partial \sigma^s_{yz}}{\partial y} + \frac{\partial \sigma^s_{zz}}{\partial z}||_2^2$.

Nonlinear Constitutive Equations The stress and displacement gradients are further constrained by the constitutive equation as $\boldsymbol{\sigma}^s = \mu_s J_s^{-1}(\mathbf{F}_s \mathbf{F}_s^\mathsf{T} - \mathbf{I}_{3\times3}) + \lambda_s(J_s - 1)\mathbf{I}_{3\times3}$, where $\mathbf{F}_s = \mathbf{I}_{3\times3} + \frac{\partial \mathbf{d}_s}{\partial \mathbf{p}_s} \in \mathbb{R}^{3\times3}$ is the deformation gradient at $\mathbf{p}_s$, $J_s = \det(\mathbf{F}_s) \in \mathbb{R}$ is the determinant of $\mathbf{F}_s$, $\lambda_s \in \mathbb{R}$ and $\mu_s \in \mathbb{R}$ are Lame parameters at $\mathbf{p}_s$ which are computed with Young's Modulus E_s and Possion's ratio v_s using $\lambda_s = \frac{E_s \nu_s}{(1-2\nu_s)(1+\nu_s)}$ and $\mu_s = \frac{E_s}{2(1+\nu_s)}$. The PDEs that comprise $\mathcal{L}^k_C(\theta; \mathcal{D}_k)$ in Eqs. (1) and (2) are $f_{\text{const}}(\boldsymbol{\sigma}^s, \frac{\partial \mathbf{d}_s}{\partial \mathbf{p}_s}, \lambda_s, \mu_s) = \sum_{i\in\{1,2,3\}} ||\sigma^s_{ii} - \mu_s J_s^{-1}((\mathbf{F}_s \mathbf{F}_s^\mathsf{T})_{ii} - 1) + \lambda_s(J_s - 1)||_2^2 + \sum_{\langle i,j\rangle \in \{\langle 1,2\rangle, \langle 1,3\rangle, \langle 2,3\rangle\}} ||\sigma^s_{ij} - \mu_s J_s^{-1}(\mathbf{F}_s \mathbf{F}_s^\mathsf{T})_{ij}||_2^2$, where to maintain uniformity of notations here $\sigma^s_{11} = \sigma^s_{xx}$ (similar for index pairs $\langle 2,2\rangle$ and $\langle 3,3\rangle$) and $\sigma^s_{12} = \sigma^s_{xy}$ (similar for index pairs $\langle 1,3\rangle$ and $\langle 2,3\rangle$) hold.

Nonlinear Elastic Energy Density Function The elastic energy function $f_{\text{energy}}(\boldsymbol{\varepsilon}^s, \lambda_s, \mu_s)$ that forms $\mathcal{L}^k_E(\theta_h; \mathcal{D}_k)$ in Eqs. (1) and (2) is $f_{\text{energy}}(\boldsymbol{\varepsilon}^s, \lambda_s, \mu_s) = \frac{\mu_s}{2}\Big(\text{tr}(\mathbf{F}_s \mathbf{F}_s^\mathsf{T}) - 3 - 2\ln J_s\Big) + \frac{\lambda_s}{2}\big(J_s - 1\big)^2\Big)$ with $\text{tr}(\mathbf{F}_s \mathbf{F}_s^\mathsf{T})$ represented by $\boldsymbol{\varepsilon}^s$.

3 Experiments and Results

Data Sets and Evaluation Metrics The dataset contains $N_k = 22$ pairs of point sets generated over MRI-derived prostate meshes [2] by producing ground-truth deformations in $[5.58, 8.66]$ mm using the finite element modelling (FEM) process, proposed in [6,21], with different material properties assigned to peripheral zones (PZ) and transition zone (TZ): the ratios of Youngs' Modulus with PZ and TZ $\frac{E^{\text{PZ}}_k}{E^{\text{TZ}}_k}$ were in the range of $[0.10, 0.20]$. All data was resampled to isotropic resolutions being $1 \times 1 \times 1$ mm^3. For each patient, the pairs of point

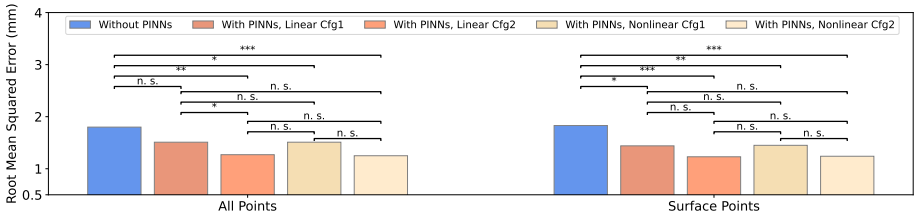

Fig. 2. The root-mean-squared-error (rmse) of registration using different algorithms for surface and all points on the left and right subplots, respectively. n.s.: not significant, $\star : p < 0.05$, $\star\star : p < 0.01$, $\star\star\star : p < 0.001$.

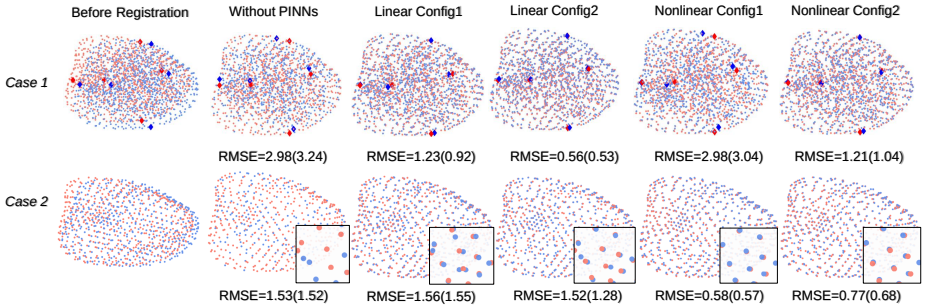

Fig. 3. Qualitative results for two cases with the five registration models. The rmse values for all points are also reported followed by those in parentheses for surface points.

sets were randomly downsampled to $\mathbf{P}_{\mathcal{S}}$ and $\mathbf{P}_{\mathcal{T}}$ with $N_s = N_t = 1024$ and $N_s^{\text{surface}} = N_t^{\text{surface}} = 512$ independently. In the first experiment, the root-mean-square error (rmse) of registration was defined between predicted displacement and ground-truth $\mathbf{D}_{\mathcal{S}}^{gt} \in \mathbb{R}^{|\widetilde{N}_s| \times 3}$ as $\text{rmse} = \sqrt{\frac{1}{|\widetilde{N}_s|} \sum_{s \in \widetilde{N}_s} ||\mathbf{d}_s - \mathbf{d}_s^{\text{gt}}||_2^2}$ where here $\widetilde{N}_s$ denote the set of all or surface points. In the second experiment, we computed the absolute percentage error (APE) as $|(\text{ratio}_{\text{pred}} - \text{ratio}_{\text{gt}})/\text{ratio}_{\text{gt}}|$ for each case where $\text{ratio}_{\text{pred}}$ and ratio_{gt} are predicted and ground-truth ratios, and also reported mean APE (mAPE) for all cases. Details about implementations such as network architectures are in the Supplementary material.

Registration Performances Fig. 2 includes the rmse values for all and surface points, respectively. Several key observations can be made from Fig. 2: (1) except for the case with Linear Cfg1 [14] for all points ($p = 0.083$), all methods outperformed Without PINNs significantly at $\alpha = 0.05$ level; (2) except for the case where Linear Cfg1 and Linear Cfg2 were significantly different for all points ($p = 0.0496$), the differences between every pair of PINNs algorithms were not statistically significant; (3) Nonlinear Cfg2 achieved the lowest mean registration error values being 1.25 ± 0.62 mm and 1.24 ± 0.68 mm for both all and surface points ($p < 0.001$), against 1.80 ± 0.44 mm and 1.83 ± 0.51 mm Without PINNs.

Fig. 3 shows the registration performances with two patient cases where blue

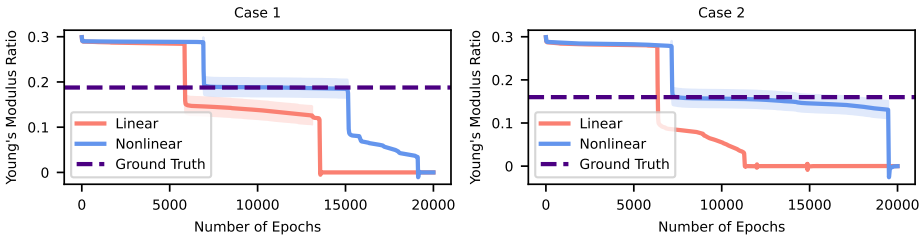

Fig. 4. The optimisation process of the inverse problem estimating the young's modulus ratio between two sub-regions of prostate, are found by locating saddle points.

Table 1. Young's modulus ratio between the two regions estimated with two models.

Patient ID	Ground-truth Ratio	Predicted Ratio Linear	APE Linear	Predicted Ratio Nonlinear	APE Nonlinear
Case 1	0.19	0.12	36.84%	**0.19**	**1.23%**
Case 2	0.16	0.10	37.50%	**0.16**	**1.25%**
Case 3	0.11	0.22	100.00%	**0.10**	**9.09%**
Case 4	0.12	0.22	83.33%	**0.15**	**25.00%**
Case 5	0.17	0	100.00%	**0.19**	**11.76%**
Case 6	0.19	0	100.00%	**0.12**	**36.84%**

and red dots respectively denote source (or predicted warped source) and target point sets with exact correspondences before (or after) registration. In *Case 1*, the linear model (e.g., rmse values were 0.56 mm and 0.53 mm for all and surface points using Linear Cfg2) was better than the nonlinear model (e.g., rmse values were 1.21 mm and 1.04 mm using Nonlinear Cfg2) and Without PINNs (i.e., rmse values were 2.98 mm and 3.24 mm), while nonlinear models outperformed linear ones and Without PINNs for *Case 2*. In the first row of Fig. 3, blue and red star shapes denote corresponding targets in two spaces.

Results of the Inverse Problem Fig. 4 demonstrates that the ratios of young's modulus between the PZ and TZ were recovered (only Cfg1s are reported due to much better performances than Cfg2s), by locating saddle points (i.e., through finding the flat line in Fig. 4) during optimisation. The confidence interval is represented as shadow area in Fig. 4. As shown in Fig. 4, the nonlinear model exhibited significant advantages which is expected because more subtle (i.e., high-order) information is preserved. Table 1 shows the ground-truth and predicted ratios for example cases, from which the APE was computed. The mAPE values with linear and nonlinear models were $76.28\% \pm 30.97\%$ and $14.20\% \pm 14.12\%$ respectively, indicating the nonlinear model performed better in the inverse problem ($p = 0.002$).

4 Discussions and Conclusions

We have demonstrated the success of incorporating the nonlinear elasticity in both forward and inverse problems of biomechanically constrained nonrigid point

set registration. This work needs to be interpreted with limitations. First, the drawn conclusions may not be directly generalizable given the limited data size. Second, although results shed light on tackling the inverse problem along with the registration, it requires additional efforts (e.g., adding regularization terms) to further improve both accuracy and success rate.

To conclude, in this paper, we have utilised PINNs to solve both the registration of soft tissues and the estimation of material properties, tackled as forward and inverse problems respectively, considering both linear and more complex nonlinear elasticities. Experimental results first show that no statistical significance is observed between linear and nonlinear models in the forward problem, among which results are highly variable across patients. The validity of adopting PINNs for solving estimating parameters, together with the superiority of the nonlinear model, is also demonstrated. These conclusions are drawn based on clinical data from prostate cancer patients, for topical applications including intraoperative motion modelling and multimodal image registration, potentially, new applications in better characterisation of pathological tissue motion.

Acknowledgments. This work was supported by the Wellcome/EPSRC Centre for Interventional and Surgical Sciences [203145Z/16/Z] and the International Alliance for Cancer Early Detection, an alliance between Cancer Research UK [C28070/A30912; C73666/A31378], Canary Center at Stanford University, the University of Cambridge, OHSU Knight Cancer Institute, University College London and the University of Manchester. This work was also supported in part by the National Natural Science Foundation of China under Grant 62303275.

Disclosure of Interests. The authors have no competing interests to declare that are relevant to the content of this article.

References

1. Fu, Y., Lei, Y., Wang, T., Patel, P., Jani, A.B., Mao, H., Curran, W.J., Liu, T., Yang, X.: Biomechanically constrained non-rigid mr-trus prostate registration using deep learning based 3d point cloud matching. Medical image analysis **67**, 101845 (2021)
2. Hamid, S., Donaldson, I.A., Hu, Y., Rodell, R., Villarini, B., Bonmati, E., Tranter, P., Punwani, S., Sidhu, H.S., Willis, S., et al.: The smarttarget biopsy trial: a prospective, within-person randomised, blinded trial comparing the accuracy of visual-registration and magnetic resonance imaging/ultrasound image-fusion targeted biopsies for prostate cancer risk stratification. European urology **75**(5), 733–740 (2019)
3. Hartmann, S., Gilbert, R.R.: Identifiability of material parameters in solid mechanics. Archive of Applied Mechanics **88**, 3–26 (2018)
4. Holzapfel, G.A.: On large strain viscoelasticity: continuum formulation and finite element applications to elastomeric structures. International Journal for Numerical Methods in Engineering **39**(22), 3903–3926 (1996)
5. Hu, Y., Ahmed, H.U., Taylor, Z., Allen, C., Emberton, M., Hawkes, D., Barratt, D.: Mr to ultrasound registration for image-guided prostate interventions. Medical image analysis **16**(3), 687–703 (2012)

6. Hu, Y., Carter, T.J., Ahmed, H.U., Emberton, M., Allen, C., Hawkes, D.J., Barratt, D.C.: Modelling prostate motion for data fusion during image-guided interventions. IEEE transactions on medical imaging **30**(11), 1887–1900 (2011)
7. Hu, Y., Modat, M., Gibson, E., Li, W., Ghavami, N., Bonmati, E., Wang, G., Bandula, S., Moore, C.M., Emberton, M., et al.: Weakly-supervised convolutional neural networks for multimodal image registration. Medical image analysis **49**, 1–13 (2018)
8. Ji, Y., Ruan, L., Ren, W., Dun, G., Liu, J., Zhang, Y., Wan, Q.: Stiffness of prostate gland measured by transrectal real-time shear wave elastography for detection of prostate cancer: a feasibility study. The British journal of radiology **92**(1097), 20180970 (2019)
9. Karniadakis, G.E., Kevrekidis, I.G., Lu, L., Perdikaris, P., Wang, S., Yang, L.: Physics-informed machine learning. Nature Reviews Physics **3**(6), 422–440 (2021)
10. Luo, J., Frisken, S., Wang, D., Golby, A., Sugiyama, M., Wells III, W.: Are registration uncertainty and error monotonically associated? In: Medical Image Computing and Computer Assisted Intervention–MICCAI 2020: 23rd International Conference, Lima, Peru, October 4–8, 2020, Proceedings, Part III 23. pp. 264–274. Springer (2020)
11. Luo, J., Ma, G., Haouchine, N., Xu, Z., Wang, Y., Kapur, T., Ning, L., Wells, W.M., Frisken, S.: On the dataset quality control for image registration evaluation. In: International Conference on Medical Image Computing and Computer-Assisted Intervention. pp. 36–45. Springer (2022)
12. Mihai, L.A., Goriely, A.: How to characterize a nonlinear elastic material? a review on nonlinear constitutive parameters in isotropic finite elasticity. Proceedings of the Royal Society A: Mathematical, Physical and Engineering Sciences **473**(2207), 20170607 (2017)
13. Miller, K., Chinzei, K.: Mechanical properties of brain tissue in tension. Journal of biomechanics **35**(4), 483–490 (2002)
14. Min, Z., Baum, Z., Saeed, S.U., Emberton, M., Barratt, D.C., Taylor, Z.A., Hu, Y.: Non-rigid medical image registration using physics-informed neural networks. arXiv preprint arXiv:2302.10343 (2023)
15. Nava, A., Mazza, E., Furrer, M., Villiger, P., Reinhart, W.: In vivo mechanical characterization of human liver. Medical image analysis **12**(2), 203–216 (2008)
16. Ogden, R.: Non-Linear Elastic Deformations. Courier Corporation (2013)
17. Pfeiffer, M., Riediger, C., Leger, S., Kühn, J.P., Seppelt, D., Hoffmann, R.T., Weitz, J., Speidel, S.: Non-rigid volume to surface registration using a data-driven biomechanical model. In: International Conference on Medical Image Computing and Computer-Assisted Intervention. pp. 724–734. Springer (2020)
18. Qi, C.R., Su, H., Mo, K., Guibas, L.J.: Pointnet: Deep learning on point sets for 3d classification and segmentation. In: Proceedings of the IEEE conference on computer vision and pattern recognition. pp. 652–660 (2017)
19. Qin, C., Wang, S., Chen, C., Bai, W., Rueckert, D.: Generative myocardial motion tracking via latent space exploration with biomechanics-informed prior. Medical Image Analysis **83**, 102682 (2023)
20. Raissi, M., Perdikaris, P., Karniadakis, G.E.: Physics-informed neural networks: A deep learning framework for solving forward and inverse problems involving nonlinear partial differential equations. Journal of Computational physics **378**, 686–707 (2019)
21. Saeed, S.U., Taylor, Z.A., Pinnock, M.A., Emberton, M., Barratt, D.C., Hu, Y.: Prostate motion modelling using biomechanically-trained deep neural networks on

unstructured nodes. In: International Conference on Medical Image Computing and Computer-Assisted Intervention. pp. 650–659. Springer (2020)
22. Taylor, Z.A., Cheng, M., Ourselin, S.: High-speed nonlinear finite element analysis for surgical simulation using graphics processing units. IEEE transactions on medical imaging **27**(5), 650–663 (2008)
23. Taylor, Z.A., Comas, O., Cheng, M., Passenger, J., Hawkes, D.J., Atkinson, D., Ourselin, S.: On modelling of anisotropic viscoelasticity for soft tissue simulation: Numerical solution and gpu execution. Medical image analysis **13**(2), 234–244 (2009)
24. van de Ven, W.J., Hu, Y., Barentsz, J.O., Karssemeijer, N., Barratt, D., Huisman, H.J.: Biomechanical modeling constrained surface-based image registration for prostate mr guided trus biopsy. Medical physics **42**(5), 2470–2481 (2015)
25. Wittek, A., Hawkins, T., Miller, K.: On the unimportance of constitutive models in computing brain deformation for image-guided surgery. Biomechanics and modeling in mechanobiology **8**, 77–84 (2009)
26. Xu, Z., Luo, J., Lu, D., Yan, J., Frisken, S., Jagadeesan, J., Wells III, W.M., Li, X., Zheng, Y., Tong, R.K.y.: Double-uncertainty guided spatial and temporal consistency regularization weighting for learning-based abdominal registration. In: Medical Image Computing and Computer Assisted Intervention–MICCAI 2022: 25th International Conference, Singapore, September 18–22, 2022, Proceedings, Part VI. pp. 14–24. Springer (2022)
27. Xu, Z., Luo, J., Yan, J., Li, X., Jayender, J.: F3rnet: full-resolution residual registration network for deformable image registration. International journal of computer assisted radiology and surgery **16**(6), 923–932 (2021)
28. Zeng, Q., Fu, Y., Tian, Z., Lei, Y., Zhang, Y., Wang, T., Mao, H., Liu, T., Curran, W.J., Jani, A.B., et al.: Label-driven magnetic resonance imaging (mri)-transrectal ultrasound (trus) registration using weakly supervised learning for mri-guided prostate radiotherapy. Physics in Medicine & Biology **65**(13), 135002 (2020)